A quantum dynamical study of the rotation of the dihydrogen ligand in the $Fe(H)_2(H_2)(PEtPh_2)_3$ coordination complex

Megan E. Gonzalez, Juergen Eckert, Adelia J. A. Aquino, and Bill Poirier

Citation: The Journal of Chemical Physics 148, 154303 (2018); doi: 10.1063/1.5026637

View online: https://doi.org/10.1063/1.5026637

View Table of Contents: http://aip.scitation.org/toc/jcp/148/15

Published by the American Institute of Physics

Articles you may be interested in

Density functional tight-binding and infrequent metadynamics can capture entropic effects in intramolecular hydrogen transfer reactions

The Journal of Chemical Physics 148, 154101 (2018); 10.1063/1.5021359

MCTDH on-the-fly: Efficient grid-based quantum dynamics without pre-computed potential energy surfaces The Journal of Chemical Physics **148**, 134116 (2018); 10.1063/1.5024869

Entangled trajectories Hamiltonian dynamics for treating quantum nuclear effects

The Journal of Chemical Physics 148, 144106 (2018); 10.1063/1.5022573

Extension of the D3 dispersion coefficient model

The Journal of Chemical Physics 147, 034112 (2017); 10.1063/1.4993215

Communication: Density functional theory model for multi-reference systems based on the exact-exchange hole normalization

The Journal of Chemical Physics 148, 121101 (2018); 10.1063/1.5025334

Communication: On the calculation of time-dependent electron flux within the Born-Oppenheimer approximation: A flux-flux reflection principle

The Journal of Chemical Physics 147, 241101 (2017); 10.1063/1.5011807



ADVANCED LIGHT CURE ADHESIVES

Take a closer look at what these environmentally friendly adhesive systems can do





A quantum dynamical study of the rotation of the dihydrogen ligand in the Fe(H)₂(H₂)(PEtPh₂)₃ coordination complex

Megan E. Gonzalez, Juergen Eckert, Adelia J. A. Aquino, and Bill Poirier Department of Chemistry and Biochemistry, and Department of Physics, Texas Tech University, P.O. Box 41061, Lubbock, Texas 79409-1061, USA

(Received 22 February 2018; accepted 3 April 2018; published online 19 April 2018)

Progress in the hydrogen fuel field requires a clear understanding and characterization of how materials of interest interact with hydrogen. Due to the inherently quantum mechanical nature of hydrogen nuclei, any theoretical studies of these systems must be treated quantum dynamically. One class of material that has been examined in this context are dihydrogen complexes. Since their discovery by Kubas in 1984, many such complexes have been studied both experimentally and theoretically. This particular study examines the rotational dynamics of the dihydrogen ligand in the Fe(H)₂(H₂)(PEtPh₂)₃ complex, allowing for full motion in both the rotational degrees of freedom and treating the quantum dynamics (QD) explicitly. A "gas-phase" global potential energy surface is first constructed using density functional theory with the Becke, 3-parameter, Lee-Yang-Parr functional; this is followed by an exact QD calculation of the corresponding rotation/libration states. The results provide insight into the dynamical correlation of the two rotation angles as well as a comprehensive analysis of both ground- and excited-state librational tunneling splittings. The latter was computed to be 6.914 cm⁻¹—in excellent agreement with the experimental value of 6.4 cm⁻¹. This work represents the first full-dimensional *ab initio* exact QD calculation ever performed for dihydrogen ligand rotation in a coordination complex. *Published by AIP Publishing*. https://doi.org/10.1063/1.5026637

I. INTRODUCTION

Within the past few decades, there has been a societal push toward cleaner energy and, more specifically, efficient and safe hydrogen fuel technologies. 1-3 *Pure* hydrogen combustion results in only water as a product—i.e., no carbon is involved. Moreover, based on the mass:energy ratio, hydrogen has nearly three times the gravimetric energy density of gasoline. 4 While the ultimate widespread utilization of hydrogen as a fuel is indeed highly desirable as a fundamentally clean energy source, many associated technical problems have yet to be adequately solved for this to become practical in reality. Among other issues is the need to store large quantities of hydrogen gas in a small volume under ambient conditions with facile uptake and release kinetics.

Porous materials with extremely large surface areas—such as metal-organic frameworks (MOFs)^{3,5,6}—satisfy most of these requirements, except for the fact that the relatively weak binding of hydrogen by physisorption requires low temperatures for their operation. Much stronger binding of hydrogen can in principle be obtained by molecular chemisorption—or the coordination of dihydrogen to metal centers, as discovered by Kubas in 1984⁷—if incorporated within materials with high surface areas. Accordingly, there has been a particular interest in the utilization of hydride metal systems such as dihydrogen complexes in the development of attractive materials for hydrogen storage.^{2,8} In any event, the significance of the discovery of dihydrogen binding now extends well beyond its fundamental importance⁹ to areas of enormous practical consequence such as

catalytic hydrogenation, ^{1,10} hydrogen storage, ¹¹ and hydrogenase function. ¹²

By now, hundreds of dihydrogen complexes have been synthesized, and extensively characterized, mainly by NMR methods, single crystal neutron or X-ray diffraction, and chemical reactivity studies. The focus of much of this work has been of a structural nature—e.g., to establish dihydrogen coordination and to determine the degree of H-H bond activation from the measured dihydrogen bond lengths. This information is most reliably derived from NMR studies of the J_{HD} coupling in partially deuterium exchanged systems¹³ since diffraction studies can be hampered by the large degree of delocalization of the hydrogen atoms. This is particularly true for transition metal polyhydrides with both dihydrogen and hydride ligands on the same metal, 14 which can in some cases rapidly interchange. This type of reaction is important for describing hydrogen spillover in catalytic reactions, and more recently, also in systems that utilize spillover under saturated conditions to increase hydrogen storage capacities at ambient temperatures^{11,15,16} relative to what is possible via physisorption alone.

In fact, the incorporation of some open metal sites for molecular hydrogen coordination in porous materials has been proposed to be the crucial step in making sorption based materials viable systems for hydrogen storage at ambient temperature, since this type of binding can easily achieve the necessary heats of adsorption above those of simple physisorption, as some recent experimental studies have shown. Nonetheless, significant progress in this important application requires a thorough understanding and characterization of how

hydrogen interacts with those materials on an atomic level scale. This requires detailed studies of the dynamics of the adsorbed or bound hydrogen molecules, along with structural results, combined together in high level computational studies. Here it is of particular importance to note that the dynamics of hydrogen, being the lightest element, are inherently of quantum mechanical nature and must be treated accordingly. It is therefore remarkable that very few previous studies of hydrogen-material interactions have incorporated quantum dynamics (QD)^{18–27}—apart from those that deal only with the quantum rotation of the H₂ molecule.²⁸

There has, of course, been much interest in the behavior of the dihydrogen ligand from the time that Kubas et al. first reported their findings of a (η^2-H_2) ligand in a coordination compound, 14,29-36 and, as a result, many one dimensional (1-D) and some two dimensional (2-D) QD models have been used to analyze the dihydrogen dynamics. 14,37-39 Models with just one rotational degree of freedom (d.o.f.) (phenomenological as well as *ab initio*) were shown⁴⁰ to be an adequate representation of the reorientation of the dihydrogen ligand, as the strong metal-dihydrogen interaction should keep the molecule confined to a plane as it rotates. Previous 2-D models for dihydrogen complexes, however, did not use ab initio methods because of the difficulty in deriving such a potential energy surface (PES).³⁹ Physisorbed hydrogen, on the other hand, always retains two rotational degrees of freedom because of the weak binding, and its rotation has generally been treated by 2-D QD, either using a phenomenological approach or a potential energy surface (PES) derived via ab initio or force field methods.41

One of the main goals of this work, accordingly, has been to provide the first ever comprehensive *ab initio* QD study of the 2-D rotation dynamics of the dihydrogen ligand in a metal complex. For this study, we have chosen the Fe(H)₂(H₂)(PEtPh₂)₃ coordination complex primarily because of the extensive amount of previous work that has been carried out on this compound ^{14,39,42,43} but also because the presence of additional hydride ligands gives rise to exchange with the dihydrogen—which we plan to study with high dimensional QD in the future. The Fe(H)₂(H₂)(PEtPh₂)₃ complex also has a unique staggered structure that is tied to its fluxional behavior. The most recent computational study was performed by Došlić *et al.* ¹⁴ in 2011. They analyzed the dihydrogen rotation in 1-D for both partially and fully optimized Fe(H)₂(H₂)(PEtPh₂)₃, in the gas phase.

This study examines the Fe coordination compound, Fe(H)₂(H₂)(PEtPh₂)₃, in the gas phase, with the goal of establishing a better understanding of the rotational QD of the H₂ ligand by including the second rotational degree of freedom (d.o.f.). Two separate QD calculations are performed, one for each of the two accurate *ab initio* potential energy surfaces (PESs) determined in this work: relaxed and (mostly) frozen. To our knowledge, there has not been a comprehensive rotational (2-D) QD study for any dihydrogen ligand in a metal complex prior to this study. This work uncovers several unexpected dynamical features, such as the highly asymmetric nature of azimuthal libration, and also significant correlation between in-plane and out-of-plane rotational motion—which manifests as "wobbling" and/or snaking of the

minimum energy path (MEP) for hindered rotation. We also report ground and excited state tunneling splittings as well as an unexpected strong Fermi resonance. Ultimately, these details may prove important for facilitating the exchange with the nearby hydride ligands, but as mentioned this remains a question for future investigations.

II. THEORY AND BACKGROUND

A. Dihydrogen complexes and the barrier to (1-D azimuthal) H₂ rotation

The discovery by Kubas et al. that molecular hydrogen (H₂) can form an η^2 " σ complex" is widely viewed as a key development in inorganic chemistry within the last two decades of the 20th century. ^{2,14,34,40} In addition to their potential in the field of clean energy, dihydrogen complexes also present the opportunity to examine a complex hindered rotor model.^{32,40} A key indicator for the coordination of hydrogen in molecular form is the observation of the transitions of the hindered rotations of the dihydrogen ligand by inelastic neutron scattering (INS) spectroscopy. These transitions can be interpreted by phenomenological models (1-D reorientation in a double-minimum potential) where the barrier to rotation is determined in a fitting procedure.⁴⁰ Alternatively, electronic structure calculations have shown the barrier to be of largely direct electronic origin³²—in contrast to the case of physisorbed hydrogen, where the barrier arises entirely from nonbonded interactions.²⁸

The origin of the electronic interaction is the overlap of the respective molecular orbitals of the metal and the dihydrogen. 40 The dominant interaction is donation from the filled σ orbital of the dihydrogen to an unfilled, symmetric d orbital on the metal, and this is accompanied by back donation to the H₂ $\sigma_{({\rm H_2})}^*$ orbital. The latter interaction requires that the d orbitals $(d_{yz} \text{ or } d_{xz})$ on the metal must be filled.³⁹ This results in the highest of the two occupied orbitals determining the preferred orientation. This is partially due to the orbital being the closest in energy to the accepting $\sigma_{({\rm H_2})}^*$. In the case that both the d_{yz} and d_{xz} orbitals are filled, the result is no strongly preferred orientation. Therefore, the barrier between the two conformations is relatively small (generally < 1000 cm⁻¹). This allows the two hydrogen nuclei to go through large amplitude librational or even rotational motion, which can lead to an exchange of their positions. This is why only one peak can be observed for an H₂ ligand in ¹H NMR spectra in solution at room temperature.

The other ligands on the metal center can strongly affect the electronic state of the metal and hence the dihydrogen binding. The more basic the ligands, the more the electron density is shifted to the metal, which in turn raises the energy of the highest occupied d orbital of the complex. This will result in an increased interaction with $\sigma^*_{({\rm H}_2)}$, which can then strengthen the back-donation enough to result in cleavage of the H–H bond (an accepted mechanism for oxidative addition to form a dihydride). Similarly, π -acceptors may compete with the back donation, which also results in dihydrogen cleavage, in the more π -basic transition metals (such as group 6).

The presence of electron rich ligands also has this effect. Alternatively, strong σ -donors may impede the σ -donation from the dihydrogen, inhibiting the binding of the dihydrogen ligand. ⁴⁰

Non-bonded or steric interactions between the hydrogen atoms of the dihydrogen ligand and the atoms on nearby coligands can also affect the barrier to rotation, but seem to be appreciably less important than the electronic interactions. ⁴⁰ In principle, the barrier to rotation should be zero, if the ligands in the plane parallel to the rotation were perfectly symmetric. However, crystal structure data for W(CO)₃(H₂)(Pi-Pr₃)₂ reveal that the WP₄ structure is distorted, and at least one of the P-W-P angles bends back and away from the dihydrogen ligand.⁴⁰ This type of distortion is commonly observed for dihydrogen complexes and it rehybridizes the metal orbitals in such a way that the overlap of $\sigma_{(H_2)}^*$ shows a variation through the rotation in the plane parallel to the WP₄ fragment (i.e., azimuthal rotation). This distortion can also be influenced by steric effects or crystal packing forces. The use of different counter ions or solvent molecules in crystallization of the compound can therefore result in different molecular structures and barriers to dihydrogen rotation.

Although the above discussion pertains to a different dihydrogen compound than the $Fe(H)_2(H_2)(PEtPh_2)_3$ complex considered here, similar comments are expected to hold. In particular, a relatively small barrier to 1-D azimuthal rotation is expected, which is further reduced if the substrate is allowed to relax. This property may account for differences between crystal structure results and those of the gas phase and is used here to justify consideration of both the frozen and relaxed PES models. In any event, Fig. 1 presents the fully relaxed $Fe(H)_2(H_2)(PEtPh_2)_3$ complex geometry obtained from our density functional theory (DFT) calculations, as discussed in Sec. III A.

The rotational exchange of the two hydrogen nuclei in the dihydrogen ligand (i.e., H₂ permutation) is associated with a symmetric-double-well azimuthal PES reaction profile (illustrated, e.g., in Fig. 5). For the lowest-lying librational states,

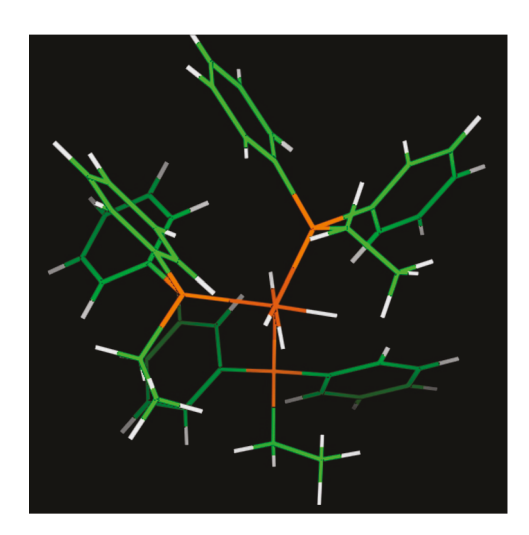


FIG. 1. Fully relaxed global minimum geometry of the gas phase $Fe(H)_2(H_2)(PEtPh_2)_3$ complex, obtained from our DFT calculations as discussed in Sec. III A. The dihydrogen ligand (front two H atoms) is rotated slightly out of its azimuthal plane.

the barrier induces a "tunneling splitting" of the hypothetical energy levels of the two identical single wells. The splitting increases rapidly with librational excitation, until it is comparable to the single-well level spacing itself, and can no longer be properly identified as "splitting" *per se*. Traditionally, this is presumed to occur near the top of the barrier, although in reality hydrogen can manifest clear "tunneling splitting" even above the barrier. ^{19,44,45} At higher energies, the librational states become rotational states, and a different dynamical picture becomes relevant. In particular, the states become fully delocalized and, at sufficiently high energies, again occur in nearly degenerate pairs—now corresponding to different linear combinations of energetically identical clockwise and counterclockwise rotations.

Figure 2 presents a rotation/libration energy level diagram for a double-well PES with a single rotational d.o.f.—the azimuthal coordinate, ϕ . As the barrier height increases, the energetic separation between the two lowest levels—i.e., the librational ground state tunneling splitting—decreases very rapidly. ^{40,46} Conversely, in the other limit, where the barrier height decreases to well below the zero-point energy, all energy levels approach those of a free rotor. The states are well labeled by the usual azimuthal quantum number, $|m| = n_{\phi}$. The lowest-lying m = 0 state is singly degenerate, but for the rotationally excited |m| > 0 states, $\pm m$ form doubly degenerate pairs.

Double-well tunneling splitting is a notoriously difficult quantity to compute with high accuracy, 45 as it is extremely sensitive to various dynamical features. Even in just 1-D, the magnitude of the splitting varies exponentially with both the height and width of the barrier. The shape of the barrier itself can also play an important role. For the Fe(H)₂(H₂)(PEtPh₂)₃ complex, in particular, the 1-D azimuthal barrier is highly asymmetric and structured (Fig. 5)—far from the broad, featureless, harmonic, or sinusoidal form adopted by standard tunneling models. The impact of the other dynamical d.o.f.'s (Sec. II B) can also be substantial, even when the direct coupling is not so strong.⁴⁷ Moreover, some tunneling splittings may be too small to be detected experimentally with the available neutron scattering instrumentation, as has been the case for the so-called stretched H–H complexes.^{32,48} In any event, for Fe(H)₂(H₂)(PEtPh₂)₃, a librational ground state

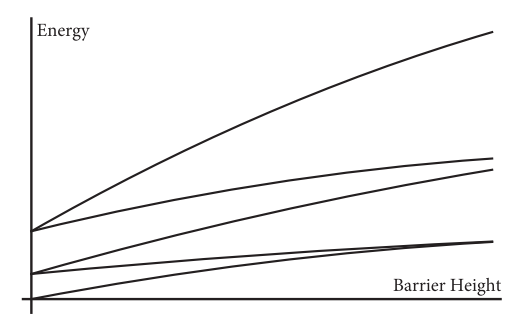


FIG. 2. Schematic indicating rotation/libration energy levels as a function of energy or rotational barrier height. 32,40 As the barrier height increases (i.e., moving to the right), the low-lying energy levels manifest in pairs that exhibit increasingly small tunneling splitting. In the opposite limit of low barrier/high energy (i.e., the left side of the figure), the energy levels pair up by azimuthal quantum number, $|m| = n_{\phi}$.

tunneling splitting was observed and found to be around 6 cm^{-1} .

B. H₂-H-H exchange and (full 2-D) H₂ rotation

A considerable number of dihydrogen complexes also possess one or more hydride ligands on the metal center, which in most cases rapidly exchange with the dihydrogen, even at very low temperatures. This process can result in a single peak for both H and H₂ in ¹H NMR spectra at high temperatures, which may decoalesce at sufficiently low temperatures into separate signals for H and H₂. ^{14,49} In other words, the hydride and dihydrogen ligands are indistinguishable at high temperatures, on account of rapid H₂-hydride exchange dynamics.⁵⁰ Many NMR studies including the one by Oldham et al.⁵⁰ on cationic iridium complexes of the form [CpIr(L)H₃]BF₄ (where $L = various Pr_3$) have clearly demonstrated this effect. As a consequence of the exchange dynamics, it becomes impossible to determine the J_{HD} coupling constant for an H-D ligand in the NMR, as well as the relaxation of the dihydrogen ligand via rotational tunneling. The barrier for exchange can be very close to that for H₂ rotation, as in the case of IrXH₂(η^2 H₂)(Pr₃)₂, but typically is found to be higher in energy.^{3,14} Normally the exchange processes would be expected to occur classically through transition states, though in previous theoretical studies these were found to be high in energy.⁴²

In any event, for the $Fe(H)_2(H_2)(PEtPh_2)_3$ complex of this study, such H_2 -hydride exchange dynamics are found to be facile, at least above room temperature. Had While such exchange dynamics will form the focus of a future QD study, here, we examine only the dihydrogen rotation dynamics, which are most relevant at lower temperatures. For the present study, the $Fe(H)_2(H_2)(PEtPh_2)_3$ coordination complex is of particular interest, due to the availability of experimental results and the depth of the studies done over the past few decades. Had, Moreover, $Fe(H)_2(H_2)(PEtPh_2)_3$, initially reported by Aresta *et al.*, is a natural extension to previous Ru and Os studies.

The most recent comprehensive study of Fe(H)₂(H₂) (PEtPh₂)₃ of which we are aware was performed by one of the authors (Eckert) and co-workers, in 2011.¹⁴ They created 1-D PES reaction profiles for both partially and fully relaxed Fe(H)₂(H₂)(PEtPh₂)₃, by varying the azimuthal coordinate (we denote " ϕ ," they denote " θ ") over 18 different points in the range $0 < \phi < \pi/2$. They performed DFT calculations using the hybrid functional Becke, 3-parameter, Lee-Yang-Parr (B3LYP), keeping the polar angle (and in the partially relaxed case, all other atoms) fixed at the crystal structure geometry. For the partially relaxed PES, they obtained a 1-D azimuthal barrier height of 332.269 cm⁻¹.

The present study examines the Fe(H)₂(H₂)(PEtPh₂)₃ complex in the gas phase, with the goal of establishing a better understanding of the H₂ rotational QD, and expands upon Eckert's 2011 work by providing a full 2-D QD rotational study, allowing both polar (θ) and azimuthal (ϕ) angles to vary freely. Formally, we define ϕ in terms of rotation in the azimuthal plane—i.e., the plane perpendicular to the Fe–H₂ vector that extends from the Fe atom to the H₂ center of mass. The polar angle θ is then defined as the angle

between the Fe-H₂ vector and the H-H vector. Separate 2-D PESs for both frozen and (fully) relaxed complex substrates are constructed, in order to ascertain which of the two dynamical pictures is more appropriate. We note that the gas phase model system likely relaxes more easily than the true crystal structure. He is can be attributed to both the crystal packing forces and the considerable intermolecular interactions. He in principle, a better approach to relaxation would include neighboring molecules—although this is unfeasible, due to the fact that a single unit cell contains close to 800 atoms. In any event, the frozen results obtained here appear to simulate the condensed phase system much better.

This 2-D study illustrates the important dynamical role played by quantum tunneling and also by θ - ϕ correlation. The latter manifests in various ways—in the snaking of the minimum energy path and resultant "wobbling" rotation, in the ground and excited state tunneling splittings, and also in the presence of Fermi resonances—all of which will be explored.

III. COMPUTATIONAL DETAILS

The basic strategy is to first compute the potential energy explicitly, using DFT, at a large number of 2-D *ab initio* geometries (θ, ϕ) . A global PES, $V(\theta, \phi)$, describing the H_2 ligand hindered rotor dynamics, is then fit to the *ab initio* data, using an expansion in spherical harmonics. Finally, using the resultant $V(\theta, \phi)$, a 2-D quantum Hamiltonian matrix is constructed, whose diagonalization provides the hindered rotor quantum eigenstates—i.e., the rotation/libration energy levels and wavefunctions. All such quantum states are computed up to $\sim 6000 \, \mathrm{cm}^{-1}$, which provides a complete characterization of the rotational QD in the energy range of interest and beyond. Analysis of the computed states then provides useful QD information, such as state labels (from wavefunction density plots), tunneling splittings, an understanding of $\theta - \phi$ correlation, etc.

A. Ab initio electronic structure calculations and global PES fits

The "ab initio" electronic structure calculations were performed by means of DFT, using the hybrid Becke, 3-parameter, Lee-Yang-Parr (B3LYP)^{52,53} functional, together with the SV(P) basis set.⁵⁴ The Stuttgart effective core potential⁵⁵ was used for the Fe atom. All calculations were carried out using the TURBOMOLE program suite.⁵⁶ As an initial test, the fully relaxed equilibrium structure was computed and compared with the previous DFT B3LYP calculations¹⁴ and also with previous crystal structure data.⁴² Select bond lengths are compared in Table I, where we note that the experimental values are from the crystal structure refinement as opposed to the gas phase structures of the calculations. The latter show a variation that is typical when using somewhat different methodologies.

The relaxed PES was constructed first. Initially, a crude PES was constructed, using 100 *ab initio* points distributed in a uniform 10×10 lattice over $0 \le \theta \le \pi$ and $0 \le \phi \le \pi$. Note that H–H permutation symmetry allows one to immediately flesh out the rest of solid angle space (corresponding to

TABLE I. Bond lengths in Å, for the global minimum geometry of the $Fe(H)_2(H_2)(PEtPh_2)_3$ complex, as obtained from one experimental source (crystal structure, column II) and two theoretical sources (gas phase DFT, columns III and IV). Hydrogen atoms H1 and H2 comprise the dihydrogen ligand, whereas H3 and H4 are the hydride ligands. In column II, the numbers in parentheses are standard deviations.

		Theory (DFT B3LYP)		
Bond	Experiment (Ref. 42)	(Ref. 14)	(Sec. III A)	
H1–H2	0.821(10)	0.844	0.820	
Fe-H1	1.576(9)	1.600	1.630	
Fe-H2	1.607(8)	1.634	1.632	
Fe-H3	1.514(6)	1.502	1.531	
Fe-H4	1.538(7)	1.509	1.532	
Fe-P1	2.162(5)	2.240	2.185	
Fe-P2	2.175(4)	2.251	2.190	
Fe-P3	2.206(4)	2.317	2.270	

 $-\pi \le \phi \le 0$) through the relation $V(\pi-\theta,\pi+\phi)=V(\theta,\phi)$. For each such *ab initio* calculation, the Fe and dihydrogen ligand geometries were frozen, and all other atoms were allowed to relax. From the resultant crude, relaxed PES, it became clear that the potential exhibits a very rapid, monotonic increase as θ varies away from the azimuthal plane—exhibiting a "polar barrier" of ~22 000 cm⁻¹ at $\theta=0$ or π . This is nearly two orders of magnitude larger than the corresponding azimuthal barrier of 248 cm⁻¹ and much beyond the dynamically relevant range. Moreover, in this most important region near the azimuthal plane, fitting errors were much larger than the target accuracy of ~10 cm⁻¹.

A much-improved relaxed PES was then constructed, as follows. First, from the crude PES, the energy contours, $V(\theta, \phi) = 2000 \text{ cm}^{-1}$, were determined [where $V(\theta, \phi)$ is taken to be zero at the minimum]. These contours are shown in the right side of Fig. 3; they represent the extreme edges of the dynamically relevant region of configuration space, denoted $\theta_{\min}(\phi)$ and $\theta_{\max}(\phi)$. Next, a set of 18 uniformly distributed ϕ values was chosen from 0 to $17\pi/18$ in increments of $\pi/18$. For each ϕ value, a ϕ -specific set of 11 uniformly distributed θ values was chosen, ranging from $\theta = \theta_{\min}$ to $\theta = \theta_{\max}$, in increments of $(\theta_{\max} - \theta_{\min})/10$. This results in a new set of 198 *ab initio* points over the most dynamically relevant region, as indicated in the left side of Fig. 3. Finally, for improved quality, one additional fixed θ value ($\theta = 1.000$) was added and paired with all 18 ϕ values, resulting in 216 points in all.

Several additional refinements of the relaxed PES were also considered, but will not be reported here.

The frozen PES was generated in a similar fashion to the improved relaxed PES described above, but with some minor differences. First, of course, none of the complex substrate atoms were allowed to relax but were instead fixed at their gas phase minimum geometry values—except for the two hydrides which were relaxed. The rationale is that the hydrides should be at least as mobile as the dihydrogen atoms—even if the other, heavier atoms are more or less "frozen" on the time scale of the dihydrogen rotation (or alternatively, if the frozen model is intended to simulate the condensed phase). Second, for reasons discussed in Sec. IV A 1, it was simpler to just use the fixed values $\theta_{\min} = 1.1108$ and $\theta_{\max} = (\pi - \theta_{\min}) = 2.0308$. The resultant 198 *ab initio* points thus flesh out a uniform rectangular lattice.

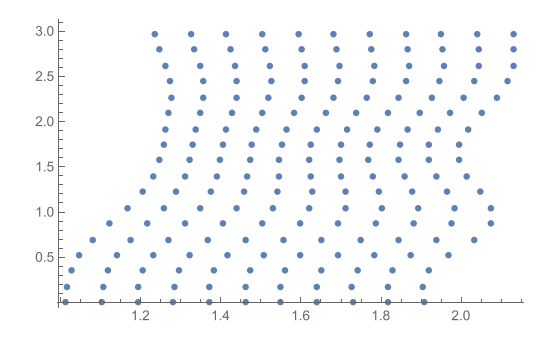
For both the relaxed and frozen PESs, it is necessary to fit a global functional form to the respective *ab initio* data (which incidentally, may be found in the supplementary material). Given the rotational, solid angle nature of the configuration space and the H–H permutation symmetry, a natural choice for the expansion functions are the spherical harmonics, $Y_{l,m}(\theta,\phi)$. In particular, due to the above-referenced H–H permutation symmetry, only even l values contribute. We therefore expand $V(\theta,\phi)$ in all even-l $Y_{l,m}(\theta,\phi)$ functions up to some maximum value l_{\max} —i.e.,

$$V(\theta, \phi) = \sum_{l=0, \text{even } m=-l}^{l_{\text{max}}} \sum_{m=-l}^{l} C_{l,m} Y_{l,m}(\theta, \phi).$$
 (1)

To determine the optimal expansion coefficients, $C_{l,m}$, for a given PES dataset, a least squares fit was applied. Three separate $l_{\rm max}$ values were considered, i.e., $l_{\rm max}=6$, 8, 10. A test of numerical convergence was then applied by comparing the resultant $V(\theta, \phi)$ functions. It was thus determined that $l_{\rm max}=8$ achieves the desired fitting accuracy of 10 cm⁻¹ or better throughout the dynamically relevant region, for both the relaxed and frozen PESs. This corresponds to an expansion in 45 spherical harmonics in all (i.e., 2l+1 for each of l=0,2,4,6,8). The set of expansion coefficients for both the relaxed and frozen PESs is provided in Table II.

B. Quantum dynamics calculations

To compute quantum eigenstates, it is necessary to represent the Hamiltonian operator, \hat{H} , as an $N \times N$ matrix, \tilde{H} , using a finite representation of N basis functions. The Hamiltonian



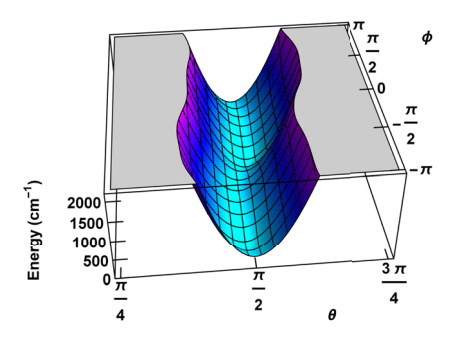


FIG. 3. (Left) The first 198 *ab initio* points comprising the improved relaxed PES dataset. θ values are generated from the 2000 cm⁻¹ contour of the crude relaxed PES. ϕ is limited to 0 to π without loss of generality, due to H–H permutation symmetry. (Right) The crude relaxed PES, $V(\theta, \phi)$, up to 2000 cm⁻¹.

TABLE II. Spherical harmonic PES expansion coefficients, $C_{l,m}$ (hartree), for the relaxed PES and the frozen PES used in this paper. Negative m coefficients are obtained from the positive m coefficients listed below, via the relation $C_{l,-m} = (-1)^m C_{l,m}^*$.

(l, m)	Relaxed PES coefficients	Frozen PES coefficients
(0,0)	0.000 750 43	0.001 072 51
(2,0)	0.124 368 81	0.125 105 29
(2,1)	$0.00492302 + 0.00509670\;i$	$0.00584281 - 0.00133842\;i$
(2,2)	0.00104825 + 0.00084952i	0.00073067 + 0.00047994i
(4,0)	0.011 059 78	0.029 820 83
(4,1)	0.00081514 + 0.00081255i	0.005 750 26 - 0.003 653 27 <i>i</i>
(4,2)	0.00007405 + 0.00011467i	0.00072651 - 0.00056940i
(4,3)	-0.00006810 + 0.00006461i	-0.00030761 + 0.00026185i
(4,4)	0.00008839 + 0.00001497i	0.00013562 + 0.00005219i
(6,0)	-0.00207226	0.007 115 50
(6,1)	0.00003020 - 0.00014154i	0.00329178 - 0.00222774i
(6,2)	0.00006740 - 0.00002356i	$0.00058482 - 0.00055547\;i$
(6,3)	0.00006254 + 0.00001391i	0.0001821 - 0.00004320i
(6,4)	$-0.00008889 - 0.00000525\ i$	-0.000 147 08 - 0.000 043 99 <i>i</i>
(6,5)	0.00002517 + 0.00000495i	-0.000 033 11 - 0.000 056 30 <i>i</i>
(6,6)	$0.00000641 - 0.00002297\;i$	0.000 001 66 - 0.000 043 43 <i>i</i>
(8,0)	-0.000 851 03	0.000 657 42
(8,1)	-0.000 063 94 - 0.000 086 52 <i>i</i>	0.000 799 64 - 0.000 622 23 <i>i</i>
(8,2)	0.00001121 - 0.00002978i	0.00015287 - 0.00020835i
(8,3)	0.00002916 + 0.00001664i	0.00009253 - 0.00003665i
(8,4)	0.00001101 - 0.00000480i	-0.000 047 04 - 0.000 021 13 <i>i</i>
(8,5)	0.00000045 + 0.00000184i	-0.000 028 86 - 0.000 051 04 <i>i</i>
(8,6)	0.00004675 - 0.00000724i	0.00004353 - 0.00004826i
(8,7)	-0.00000571 + 0.00002254i	$-0.00000802 + 0.00000510\ i$
(8,8)	0.00006930 + 0.00000459i	0.00004267 + 0.00000460i

operator is given by

$$\hat{H} = \hat{V} + \hat{T}_{\text{rot}} = V(\theta, \phi) + \frac{\hat{I}^2}{2I}, \tag{2}$$

where \hat{l}^2 is the total angular momentum, $I = \mu R_e^2$ is the dihydrogen moment of inertia, $\mu = 925.332$ a.u. is the dihydrogen reduced mass, and $R_e = 0.819~525$ Å is the H–H bond length for the gas phase minimum geometry (Table I). The representational basis is itself taken to be composed of spherical harmonics, with $\langle \theta, \phi | lm \rangle = Y_{l,m}(\theta, \phi)$.

The individual matrix elements of \tilde{H} —i.e., $H_{l,m,l',m'} = \langle lm|\hat{H}|l'm'\rangle$ —are therefore given by the following:

$$H_{l,m,l',m'} = \int Y_{l,m}^*(\theta,\phi)\hat{H} Y_{l',m'}(\theta,\phi) \sin\theta d\theta d\phi$$
$$= \langle lm \mid \hat{T}_{\text{rot}} \mid l'm' \rangle + \langle lm \mid V(\theta,\phi) \mid l'm' \rangle. \quad (3)$$

The kinetic energy contribution is particularly simple, resulting in a diagonal matrix because the $Y_{l,m}$'s are eigenstates of \hat{T}_{rot} ,

$$T_{l,m,l',m'} = \frac{\hbar^2}{2I} l(l+1)\delta_{l,l'}\delta_{m,m'}.$$
 (4)

The potential energy contribution is more complicated, as it requires a separate 2-D integral for every one of the N^2 matrix elements. On the other hand, because $V(\theta,\phi)$ is itself expressed in terms of spherical harmonics, an analytic evaluation of the $V_{l,m,l',m'}$ matrix elements is possible. In particular, one finds that

$$\langle lm \mid V(\theta, \phi) \mid l'm' \rangle = \int_{0}^{\pi} \sin \theta d\theta \int_{-\pi}^{\pi} d\phi Y_{l,m}^{*}(\theta, \phi) V(\theta, \phi)$$

$$\times Y_{l',m'}(\theta, \phi)$$

$$= \sum_{l''=0, \text{even}}^{l_{\text{max}}} \sum_{m''=-l''}^{l''} C_{l''m''} \int_{0}^{\pi} \sin \theta d\theta$$

$$\times \int_{-\pi}^{\pi} d\phi Y_{lm}^{*} Y_{l''m''} Y_{l'm'}, \qquad (5)$$

where the integrals—changing our notation slightly—become

$$\int \sin\theta d\theta \int d\phi Y_{l_3m_3}^* Y_{l_2m_2} Y_{l_1m_1}$$

$$= \left[\frac{(2l_1+1)(2l_2+1)}{4\pi(2l_3+1)} \right]^{\frac{1}{2}} C(l_1l_2l_3; m_1m_2m_3) C(l_1l_2l_3; 000).$$
(6)

Thus, the integrals in Eq. (5) can be analytically expressed in terms of Clebsch-Gordan coefficients, $C(l_1l_2l_3;m_1m_2m_3)$. In this manner, each of the N^2 matrix elements is obtained as a sum over 45 Clebsch-Gordan terms of the Eq. (6) form. In practice, this can get rather large so that evaluation of these terms becomes the computational bottleneck. To reduce the necessary computational effort, all of the necessary Clebsch-Gordan coefficients are precomputed—i.e., up to $l_{\rm MAX}=20$ for the even-l calculations and $l_{\rm MAX}=19$ for the odd-l calculations, where $l_{\rm MAX}$ is the truncation parameter that limits the size of the representational basis, via $l \le l_{\rm MAX}$.

Note that because of the H-H permutation symmetry of the Hamiltonian, the para-H₂ and ortho-H₂ quantum states can be computed separately. In particular, the para-H₂ states have even spatial symmetry and can be associated with l = even. The ortho-H₂ states have odd spatial symmetry and correspond to l = odd. To compute a finite representational Hamiltonian matrix, therefore, one uses all even-l or odd-l spherical harmonic basis functions, up to the maximum value l_{MAX} . By increasing l_{MAX} , recomputing eigenvalues and comparing with smaller l_{MAX} eigenvalues, the level of numerical convergence can be assessed. Note that the convergence is variational, meaning that all computed eigenvalues converge from above, because the representation is analytic. In this manner, it was demonstrated that using the values $l_{MAX} = 20$ and l_{MAX} = 19, for para-H₂ and ortho-H₂, respectively, the resultant computed energy eigenvalues are all basis-set converged to an accuracy of 10⁻² cm⁻¹ or better, up to a maximum energy of ~6000 cm⁻¹. Most states are far better converged.

C. Creating and analyzing wavefunction density plots

From the even and odd Hamiltonian matrices, eigenvectors are also obtained. For each eigenvector, the corresponding wavefunction is obtained by multiplying each component by the corresponding spherical harmonic function and summing. Taking the square amplitude then results in the wavefunction density. By plotting and analyzing wavefunction densities, it becomes possible to assign labels to each of the states—i.e., (n_{θ}, n_{ϕ}) —in terms of the number of excitations in θ and ϕ , respectively, based on the number of peaks that manifest in the corresponding direction. Note that $n_{\theta} + n_{\phi} = \text{even/odd}$, for

the l= even/odd calculations, respectively. In principle, this property can also aid in the label assignments, although for this particular application, almost all of the labels are straightforward. Note further that each new excitation in θ results in a new peak, whereas each new excitation in ϕ results in two new peaks, due to the periodic symmetry exhibited by the ϕ d.o.f. As discussed, these are associated with two new quantum states which become nearly degenerate in the large- n_{ϕ} limit, in which n_{ϕ} corresponds to $\pm m$. Finally, pairs of quantum states that exhibit tunneling splitting always correspond to the same n_{θ} value and adjacent n_{ϕ} values.

IV. RESULTS

A. Global PESs: relaxed vs. frozen

1. Basic features

Following the procedures described in Sec. III A, global PESs of the Eq. (1) form were constructed, for both (improved) relaxed and (mostly) frozen geometries. Plots of the relaxed and frozen PESs are indicated, respectively, in the left and right sides of Fig. 4, spanning the dynamically relevant region up to 2000 cm^{-1} . Significant $\theta - \phi$ correlation can be observed in both PESs, manifesting as a slight snaking of the azimuthal channel. The azimuthal rotational barrier can also be observed, albeit just barely.

From the figure, it is clear that the rotational dynamics are effectively restricted to a fairly narrow polar band, extending about 20° in either direction above and below the $\theta = \pi/2$ azimuthal plane. It is also clear that the improved relaxed PES turns out to exhibit less snaking/correlation than the crude relaxed PES. For this reason, when constructing the frozen PES, we simply used fixed θ limits for the lattice of *ab initio* points—rather than a varying lattice as in the left side of Fig. 3. In the event, however, it turns out that the resultant frozen PES also exhibits more snaking than the (improved) relaxed PES, particularly at the higher energies of the dynamically relevant range, near 2000 cm^{-1} . This might be attributable to the extra motions needed for the dihydrogen to move around pendant ligands that are frozen in place.

2. Reaction pathways and profiles, and azimuthal barrier heights

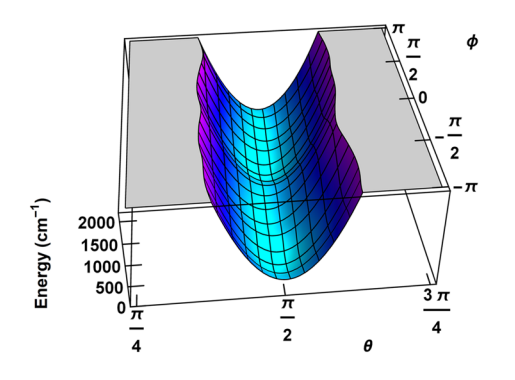
In all theoretical investigations thus far conducted, the global minimum geometry of the $Fe(H)_2(H_2)(PEtPh_2)_3$ complex exhibits a slight tilting of the dihydrogen out of the

azimuthal plane. This presents a natural question: what happens as the dihydrogen undergoes azimuthal rotation? Does the polar angle θ remain constant? H–H permutation symmetry suggests otherwise: after a 180° azimuthal rotation, θ must become $(\pi - \theta)$, in order that the two H atoms be exchanged—thus resulting in the second equivalent minimum geometry. Moreover, the pathway between the two equivalent minima—expressed as a function, $\theta(\phi)$ —need hardly be a smooth straight line.

In order to connect with previous model calculations performed on the H₂ rotational dynamics that only considered 1-D azimuthal motion, in this section, we discuss various 1-D azimuthal reaction profiles, generated from our 2-D PES's. As discussed above, the symmetry and tilted global minimum geometry provide several reasonable possibilities. The simplest is to assume strict rotation within the $\theta = \pi/2$ azimuthal plane. This is the procedure that was adopted in previous 1-D model calculations. An advantage is that the resultant reaction profile exhibits correct doubly periodic behavior. A disadvantage is that $V(\pi/2, \phi)$ passes through neither the true global minima nor the true transition states (both are overestimated). Alternatively, one can fix $\theta = \theta_{\text{equil}}$, which ensures that the reaction pathway passes through one true minimum. However, this choice does not respect H–H permutation symmetry; not only is the resultant $V(\theta_{\text{equil}}, \phi)$ not doubly periodic, but it misses the second global minimum. The third and arguably best choice is to take $\theta(\phi)$ to be the minimum energy path (MEP). This choice passes through both equivalent minima, as well as both equivalent transition states, and otherwise exhibits the desired double periodicity.

The extent to which the three reaction profiles defined above—and their associated reaction pathways—differ from each other provides a measure of the extent of θ – ϕ correlation at low energy. In Fig. 5, we present all such reaction profiles and pathways, for both the relaxed and frozen PESs. The results are somewhat interesting. For the relaxed PES, the global minima ($\theta_{\text{equil}} = 1.57151$) are in fact barely tilted from $\theta = \pi/2$ so that the $\theta = \theta_{\text{equil}}$ and $\theta = \pi/2$ reaction profiles are practically identical. On the other hand, the transition state geometry is significantly tilted, and the MEP otherwise exhibits rather convoluted snaking over a θ range of about 0.07 rad—implying significant "wobbling" in the rotational dynamics. Yet despite this, the MEP reaction profile is actually fairly close to the other two.

By contrast, the three reaction profiles for the frozen PES show more variation and are all somewhat different from each



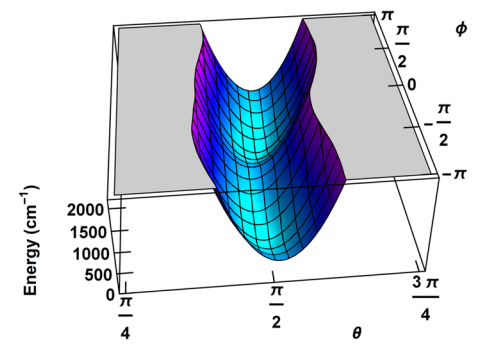


FIG. 4. Plots of the two PESs, $V(\theta, \phi)$, used in this paper to compute quantum states for dihydrogen rotation in the Fe(H)₂(H₂)(PEtPh₂)₃ complex: (left) (improved) relaxed PES; (right) frozen PES. In both cases, only the dynamically relevant region up to 2000 cm⁻¹ is indicated.

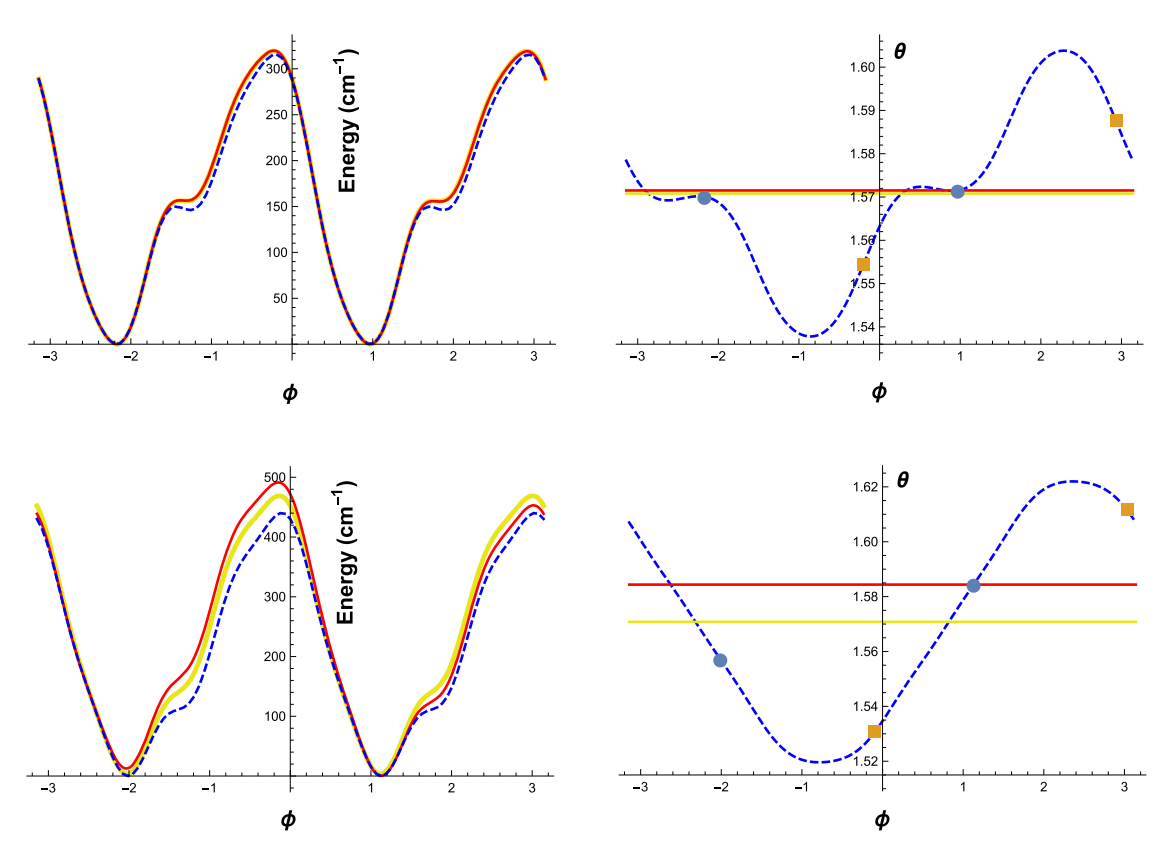


FIG. 5. (Left) Reaction profiles, $V[\theta(\phi), \phi]$, for dihydrogen rotation in the Fe(H)₂(H₂)(PEtPh₂)₃ complex, obtained using three different reaction pathways: $\theta(\phi) = \pi/2$ (yellow, solid); $\theta(\phi) = \theta_{\text{equil}}$, the value at the global minimum (red, solid); $\theta(\phi) = \text{MEP}$, the minimum energy path (blue, dashed). (Right) The three reaction pathways just described, $\theta(\phi)$, indicated in the same manner as the reaction profiles. Blue circles represent the global minima; yellow-orange squares represent the transition states (azimuthal barriers). Upper plots refer to the relaxed PES; lower plots refer to the frozen PES.

other. Here, the minimum geometry is also significantly tilted, accounting for the differences between the $\theta = \pi/2$ and $\theta = \theta_{\text{equil}}$ = 1.584 39 reaction profiles. The MEP reaction pathway spans a slightly broader θ range (about 0.10 rad) than in the relaxed PES case, although the curve itself is much smoother. This implies greater snaking or tilted rotation in the frozen case, but less wobbling. In any event, it seems that the details of the snaking—much like the resultant tunneling splitting itself depends sensitively on the PES. An additional point of interest is the symmetry of the reaction profiles that arises due to the H-H permutation symmetry. This is a translational (doubly periodic) symmetry, but not a reflection symmetry. Indeed, all reaction profiles are found to be *highly asymmetric* with respect to reflection. This effect, probably due to the steric interactions, has not been much considered in prior calculations but is clearly dynamically very significant.

In comparing the broad features of the relaxed vs. frozen PESs, these appear to be qualitatively similar to each other, especially vis-à-vis the pattern of asymmetry. On the other hand, there is one highly significant difference: the frozen PES has a *much* higher barrier height (440.410 cm⁻¹) than the relaxed PES (315.450 cm⁻¹). Note that these barrier height quantities are defined using the MEP—or equivalently, as the difference between the global minimum and transition state potential energy values. In accord with the discussion in Sec. II A, we expect the frozen PES to exhibit a substantially smaller ground state tunneling splitting—as is indeed found to be the case (Sec. IV B 2).

B. Quantum dynamics calculations: Rotation/libration states

1. Energy levels and transition frequencies

As per the discussion in Sec. III B, all para-H₂ (e) and ortho-H₂ (o) quantum rotation/libration states were computed up to $\sim 6000 \, \mathrm{cm}^{-1}$ —to an accuracy of $0.01 \, \mathrm{cm}^{-1}$ or better—for both the relaxed and frozen PESs. For every quantum state, both energy levels and wavefunctions were computed. Note that for a 2-D system, it is possible to visualize the entire wavefunction density at once. Accordingly, visual inspection of the wavefunction density plots is the simplest means of assigning (n_{θ}, n_{ϕ}) labels and is the strategy adopted here (Sec. IV B 3).

Table III reports zero-point energies, together with all excited state rotation/libration transition frequencies up to ~2000 cm⁻¹. All states indicated in the table are converged to a few 0.0001 cm⁻¹ or better. Both e and o states are merged together, in increasing energetic order. In addition to (n_{θ}, n_{ϕ}) labels, we also provide $e\{v\}$ or $o\{v\}$ labels, where $e\{v\}$ is the v'th para-H₂ state, in increasing energetic order. Results are presented for both the relaxed and frozen PESs. Although the energies and frequencies for the two PESs differ significantly from each other, the e/o ordering of excited states is exactly the same in both cases over the energy range indicated—although at higher energies, there are some differences. A comprehensive list of all computed energy levels, for both PESs, is reported in the supplementary material. All energy levels for both PESs are also represented in Fig. 6. From the figure, both

TABLE III. Zero-point energies and transition frequencies, for the ground and excited rotation/libration states, respectively, associated with dihydrogen rotation in the Fe(H)2(H2)(PEtPh2)3 complex. Columns I-III: relaxed PES; columns IV-VI: frozen PES. Energies (third column in each group) are reported in cm⁻¹. All quantum states are assigned both $e/o\{v\}$ and (n_{θ}, n_{ϕ}) labels, in the first and second column of each group, respectively.

Relaxed PES			Frozen PES		
$e/o\{v\}$	(n_{θ}, n_{ϕ})	Energy (cm ⁻¹)	e/o{ <i>v</i> }	(n_{θ}, n_{ϕ})	Energy (cm ⁻¹)
e1	(0,0)	925.580	e1	(0,0)	1043.835
o1	(0,1)	12.996	o1	(0,1)	6.914
o2	(0,1)	139.728	o2	(0,1)	187.302
e2	(0,2)	226.200	e2	(0,2)	250.218
e3	(0,2)	277.595	e3	(0,2)	338.315
o3	(0,3)	495.995	о3	(0,3)	533.938
o4	(0,3)	507.986	04	(0,3)	550.504
e4	(0,4)	851.596	e4	(0,4)	884.606
e5	(0,4)	860.338	e5	(0,4)	898.692
o5	(0,5)	1312.548	05	(0,5)	1344.482
06	(0,5)	1313.890	06	(0,5)	1347.928
o7	(1,0)	1656.367	о7	(1,0)	1868.929
e6	(1,1)	1672.627	e6	(1,1)	1877.479
e7	(1,1)	1792.892	e7	(0,6)	1903.114
e8	(0,6)	1872.147	e8	(0,6)	1903.529
e9	(0,6)	1872.388	e9	(1,1)	2054.242

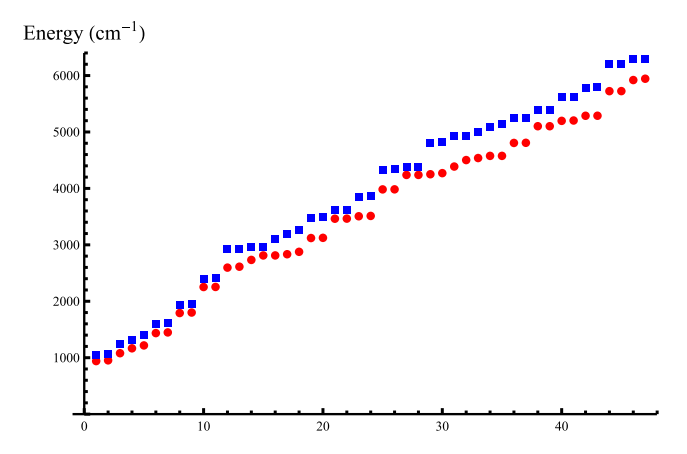


FIG. 6. Plot of all computed energy levels below ~6000 cm⁻¹, in energetic order, for the quantum rotation/libration states associated with dihydrogen rotation in the Fe(H)2(H2)(PEtPh2)3 complex: relaxed PES (red circles); frozen PES (blue squares).

the tunneling splitting near-degeneracy at low energies and the azimuthal nearly free-rotor near-degeneracy at higher energies are clearly visible.

2. Tunneling splittings and comparison with previous work

The ground state tunneling splitting corresponds to the transition $e1(0, 0) \leftarrow o1(0, 1)$. In Table IV, the transition frequencies for both the relaxed and frozen PESs of the present study are extracted from Table III and compared with previous experimental and theoretical results. The experimental data are from a neutron scattering study performed in the condensed phase by Eckert et al., 42 whereas the previous theoretical predictions are all based on 1-D azimuthal models.¹⁴

Remarkably, the 2-D frozen PES prediction of 6.914 cm⁻¹ obtained here agrees with the experimental value of 6.4 cm⁻¹ to within one half wavenumber, or less than 10%. This level of agreement is astonishing for an ab initio tunneling splitting calculation and is perhaps a bit serendipitous. On the other hand, the frozen PES predictions for the other two experimentally available transition frequencies—i.e., for $e1(0, 0) \leftarrow o2(0, 1)$ and $e1(0, 0) \leftarrow e2(0, 2)$ —also agree very well with the experimental observations. For the latter transition, the agreement is better than 2 cm^{-1} out of $\sim 250 \text{ cm}^{-1}$ —i.e., better than 1%. For $e1(0, 0) \leftarrow o2(0, 1)$, the discrepancy is nearly an order of magnitude larger—which is still excellent—and comparable to the error in the PES itself.

The above performance of the frozen PES should be compared with that of the other theoretical predictions—i.e., the relaxed PES of the present study, as well as the 1-D azimuthal model calculations performed previously, using various density functionals. In comparison with the relaxed PES, it is clear that the frozen PES performs much better. In particular, the (necessarily) lower azimuthal rotation barrier of the relaxed PES results in a much larger tunneling splitting—and much lower excited state energies—than for the frozen PES. All of the 1-D model predictions behave similarly; indeed, TPSS even achieves quantitative agreement with the relaxed PES predictions.

The above state of affairs should seem odd, considering that the 1-D models are based on frozen, not relaxed, structures. On the other hand, there is a straightforward physical explanation which is that the snaking of the azimuthal channel behaves as a de facto increase in the barrier height. Such behavior has been observed previously in quantum systems.⁵⁸ For the present $Fe(H)_2(H_2)(PEtPh_2)_3$ complex, the magnitude of this effect is evidently comparable to that of relaxing the substrate vs. keeping it frozen. In any event, the lesson seems clear: accurate modeling of the experimental data requires that both (a) frozen substrates and (b) 2-D snaking dynamics are employed.

TABLE IV. Rotation/libration transition frequencies (in cm⁻¹) for the three lowest-lying excited quantum states associated with dihydrogen rotation in the Fe(H)₂(H₂)(PEtPh₂)₃ complex. A comparison of experimental results⁴² vs. various theoretical predictions is presented (most relevant in bold face).

	Experiment ⁴²	1-D azimuthal models ¹⁴			2-D PESs (this work)	
Transition		wB97XD	B3LYP	TPSS	Relaxed	Frozen
$e1(0, 0) \leftarrow o1(0, 1)$	6.4	10.7	8.8	12.3	12.996	6.914
$e1(0, 0) \leftarrow o2(0, 1)$	170	148.4	155.4	139.1	139.728	187.302
$e1(0,0) \leftarrow e2(0,2)$	252	223.6	228.4	222.2	226.200	250.218

The 2-D QD calculations enable predictions of excited state tunneling splittings, of two different kinds. The first kind consists of the usual splittings associated with excitations in n_{ϕ} , which are expected to increase rapidly. Indeed, for the first such excited state—i.e., o2(0, 1)—the (experimental) tunneling splitting is already ~80 cm⁻¹ which is comparable to the level spacing. Moreover, the corresponding excitation energies are also comparable to the azimuthal barrier height. This suggests that for $n_{\phi} > 1$, tunneling is no longer meaningful.

The 2-D QD calculations also provide excited state tunneling splittings associated with excitations in n_{θ} . These are interesting because they provide another indication of θ - ϕ correlation: if θ and ϕ were completely decoupled, then the tunneling splittings would be independent of n_{θ} . Table V presents excited-state tunneling splittings over the ranges $n_{\phi} = \{0, 1\}$ and $n_{\theta} = \{0, 1, 2, 3\}$. Both relaxed and frozen results are presented. From the table, it is clear that increasing n_{θ} gives rise to a significant increase in the tunneling splittings for a given n_{ϕ} . This trend can be easily understood as follows: for larger n_{θ} excitations, the system explores a larger region of θ space, and so the impact of snaking (e.g., to increase the effective barrier height) becomes less significant.

2π

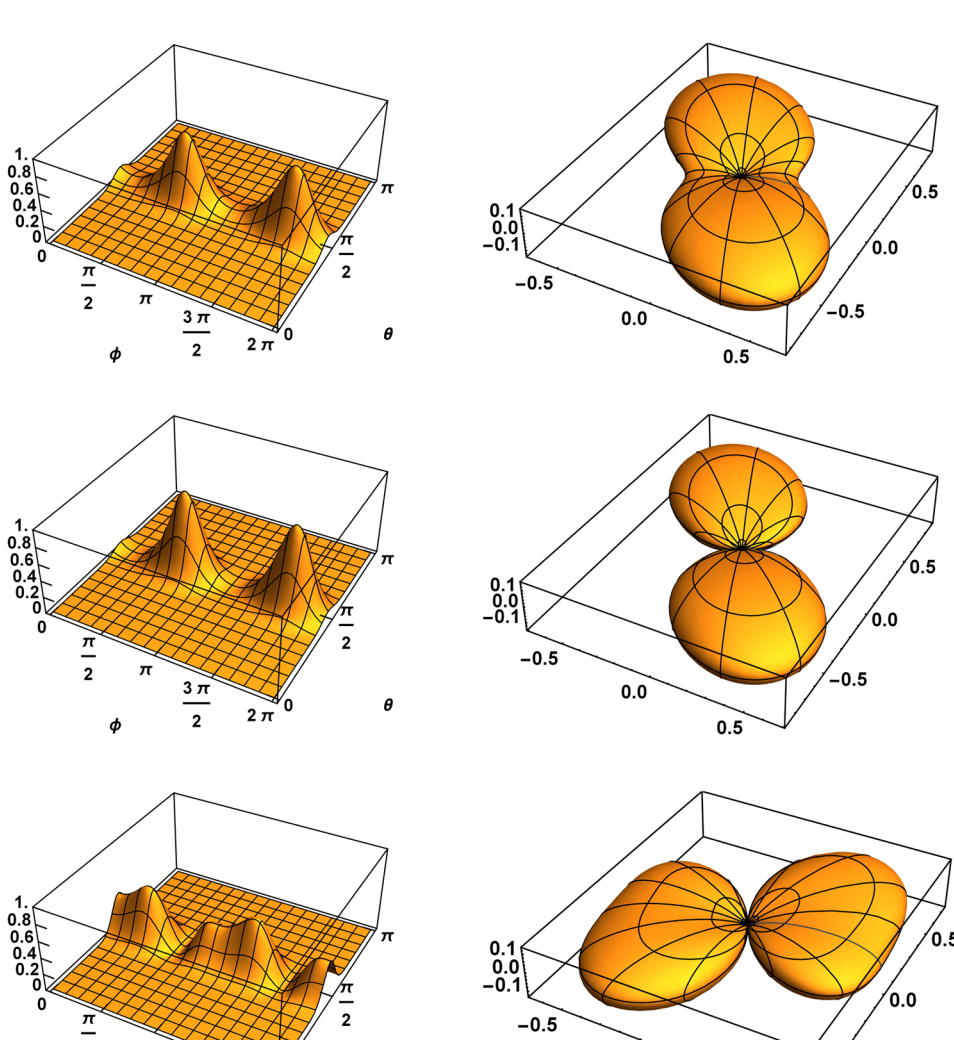
TABLE V. Ground and excited state tunneling splittings (in cm⁻¹) for dihydrogen rotation in the Fe(H)₂(H₂)(PEtPh₂)₃ complex. Excitations in both n_{θ} and n_{ϕ} are considered. Column I: $e/o(n_{\theta}, n_{\phi})$ label for the lower state of each tunneling splitting pair; column II: relaxed PES; column III: frozen PES (bold).

State label	Relaxed PES	Frozen PES	
e(0, 0)	12.996	6.914	
o(1,0)	16.260	8.550	
e(2, 0)	19.405	10.587	
o(3, 0)	23.491	12.979	
o(0, 1)	86.472	62.916	
e(1, 1)	100.655	74.548	
o(2, 1)	114.938	86.635	
e(3, 1)	130.076	100.151	

3. Wavefunction density plots

Wavefunction density plots are used to assign (n_{θ}, n_{ϕ}) labels—and additionally, to pair up states based on tunneling splitting or on $|\pm m| = n_{\phi}$ values. Wavefunction density plots are also used to identify Fermi resonances.

Figure 7 presents wavefunction density plots for the ground and first two excited rotation/libration states of the



0.0

-0.5

0.5

FIG. 7. Wavefunction density plots for the three lowest-lying rotation/libration states of the Fe(H)₂(H₂)(PEtPh₂)₃ complex, computed using the relaxed PES and presented in both rectilinear (left) and spherical (right) (θ, ϕ) views: (top) ground state, e1(0, 0); (middle) first excited state, o1(0, 1); (bottom) second excited state, o2(0, 1).

Fe(H)₂(H₂)(PEtPh₂)₃ complex, computed using the relaxed PES. On the right side of the figure, the wavefunction densities are presented in an intuitive spherical or "solid angle" space view, in which the radial distance corresponds to the relative probability that the dihydrogen is oriented in a given direction. For the ground state, for instance, we see that the dihydrogen is well localized in both θ and ϕ , about two equivalent (antipodal) geometries. Such plots are useful for geometric visualization. However, since n_{θ} and n_{ϕ} are nearly good quantum numbers, for state labeling purposes, it is also convenient to use a "rectilinear" view, as on the left side of the figure.

The ground and first excited states are tunneling splitting partners. This is clear from the fact that the pair of density peaks occur at the same location and that the first excited state has a node at the symmetric double-well barrier. Interestingly, the first and second excited states are *also* paired together, through their common $n_{\phi} = 1$ value. This is indicated by the fact that these two plots both exhibit two peaks in the azimuthal direction that are *shifted out of phase*, relative to each other. These patterns persist throughout the spectrum.

Figure 8 presents the six lowest-lying rotation/libration states of the Fe(H)₂(H₂)(PEtPh₂)₃ complex, computed using the *frozen* PES, in the rectilinear view. Here, a comparison between the second [o2(0,1)] and third [e2(0,2)] excited states is interesting. These form an excited state tunneling splitting pair and so should have peaks at the same locations—yet based on n_{ϕ} , o2(0,1) should have only two peaks and e2(0,2) should have only four peaks. An examination of the plots reveals how these conditions are satisfied. At higher energies, the patterns of peaks and nodes become more regular, for the most part. The first excitation in θ does not occur until 1870 cm⁻¹ [o7(1,0)]. Wavefunction density plots for the states of the $(n_{\theta},0)$ progression are presented in Fig. 9. Note that the high lying $(n_{\theta},0)$ states have quite large probability far from the azimuthal plane at $\theta=\pi/2$.

For the relaxed PES, Fermi resonances have been observed above 2000 cm⁻¹. Note that these always involve a *quartet* of states, since each distinct (n_{θ}, n_{ϕ}) configuration includes two states. Figure 10 presents the wavefunction density plots for the four states belonging to the lowest-lying Fermi

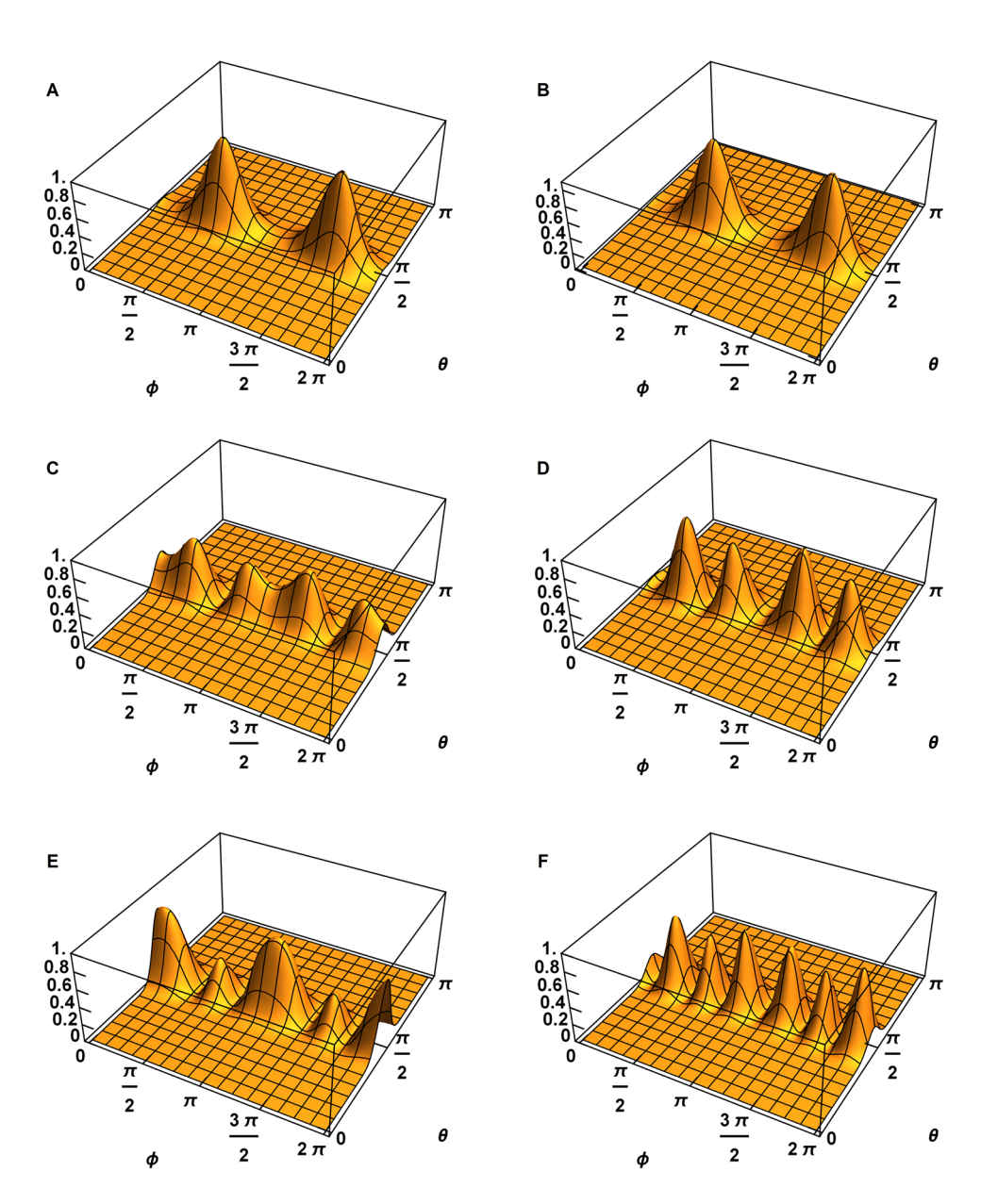


FIG. 8. Wavefunction density plots for the six lowest-lying rotation/libration states of the $Fe(H)_2(H_2)(PEtPh_2)_3$ complex, computed using the frozen PES: (a) e1(0, 0); (b) o1(0, 1); (c) o2(0, 1); (d) e2(0, 2); (e) e3(0, 2); (f) o3(0, 3).

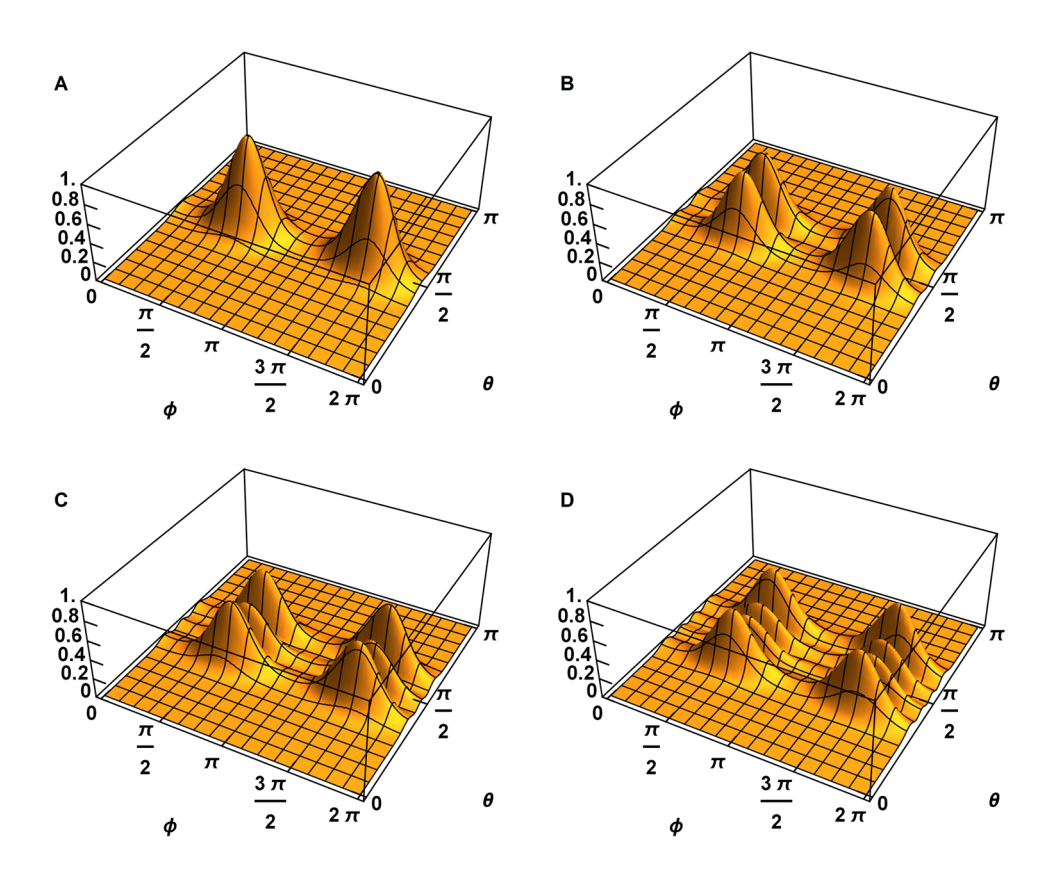


FIG. 9. Wavefunction density plots for the four lowest-lying rotation/libration states in the $(n_{\theta}, 0)$ progression of the Fe(H)₂(H₂)(PEtPh₂)₃ complex, computed using the frozen PES: (a) e1(0, 0), 0 cm⁻¹; (b) o7(1, 0), 1868.93 cm⁻¹; (c) e16(2, 0), 3754.65 cm⁻¹; (d) o26(3, 0), 5657.12 cm⁻¹.

resonance, near 2500 cm⁻¹. For these four states, the wavefunctions *themselves* exhibit a snaking pattern—indicating, once again, the effect of θ - ϕ correlation. As a consequence, the set of peaks and nodes can be interpreted in two different

ways—in this case, either as (0, 7) or as (1, 4). The frozen PES does not exhibit any Fermi resonances below 6000 cm⁻¹.

Wavefunction density plots for many high-lying states are presented in the supplementary material.

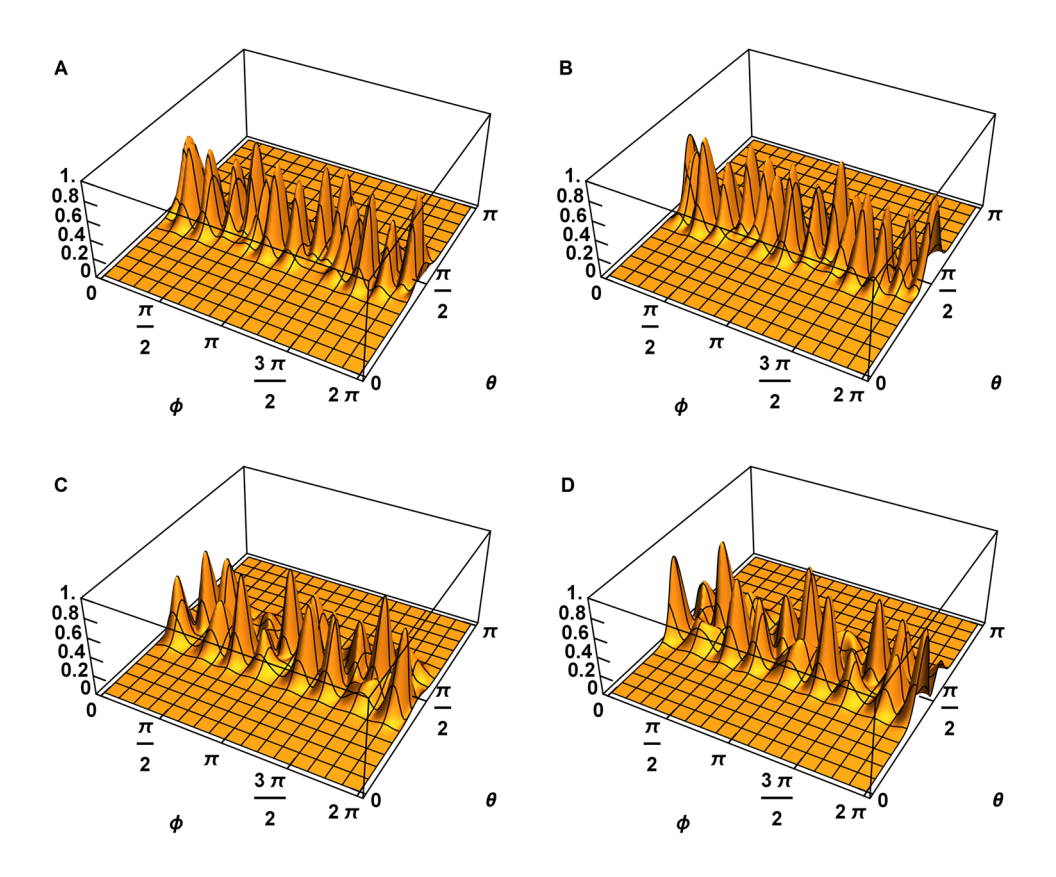


FIG. 10. Wavefunction density plots for the four rotation/libration states belonging to the lowest Fermi resonance of the Fe(H)₂(H₂)(PEtPh₂)₃ complex, computed using the relaxed PES: (a) o10, 2522.88 cm⁻¹; (b) o11, 2524.65 cm⁻¹; (c) o12, 2566.35 cm⁻¹; (d) o13, 2572.33 cm⁻¹. These states correspond to $(n_{\theta}, n_{\phi}) = (0, 7)$ and (1, 4).

V. SUMMARY AND CONCLUDING REMARKS

For fundamental as well as practical reasons, there is an interest in understanding how hydrogen—in both atomic and molecular forms—interacts with nanomaterials. The effect of the material substrate on both the hydrogen spectroscopy and reactivity is of interest. To this end, understanding the structural modifications caused by the host substrate—e.g., to the equilibrium bond length of a guest H₂ molecule, say—is obviously important. On the other hand, hydrogen—being the lightest element—does not localize at any single specific structure but tends to delocalize over many geometries. Moreover, QD effects such as tunneling can also be important. A proper characterization of hydrogen therefore requires a quantum treatment of the dynamics (i.e., nuclear motion) as well as the electronic structure.

In this study, we examine the QD of the dihydrogen ligand in the $Fe(H)_2(H_2)(PEtPh_2)_3$ complex. Above room temperature, the H₂ can interact with the two nearby hydride ligands in an interesting, complex-mediated, hydrogen exchange reaction that will serve as the focus of future work. Here, as an initial study, we examine the dynamics below room temperature, which are dominated by hindered rotation/libration of the H₂ ligand. The structure and dynamics in this context have been well characterized experimentally, through crystal structures, NMR, and neutron scattering experiments. Part of our motivation for the present study, therefore, is to assess the validity and/or limits of our full-dimensional ab initio QD methodology—which, to our knowledge, has not been applied previously to hydrogen ligands in a coordination complex (though similar calculations have been performed for H₂@C₆₀ and H_n -carbon-nanotube systems ^{18,19}).

The structural part of the present study, conducted using DFT with the B3LYP functional, is the most straightforward aspect. Our calculation of the minimum-energy structure predicts an elongated H₂ bond length of 0.820 Å, in excellent agreement with the experimental value of 0.821 Å. The computed Fe-H and Fe-P bond lengths are also in good agreement with previous experimental measurements and theoretical calculations. As for the H₂ hindered rotation dynamics, this is investigated explicitly over the full 2-D spherical rotation space. Two limiting models are considered, one in which the substrate is allowed to relax fully as the H₂ rotates and one for which it is "frozen" at the equilibrium structure. The latter is presumed to be a better model for experiments, most of which were conducted in the condensed phase—although it should be noted that we consider only gasphase structures here (as is also true of previous theoretical

Having developed new 2-D PESs for each of the two models described above, we then computed all of the corresponding rotation-libration quantum states, to very high energy (6000 cm⁻¹) and numerical convergence accuracy (10⁻⁴ cm⁻¹ for transition frequencies up to 2000 cm⁻¹). For the H₂ hindered rotational dynamics in the Fe(H)₂(H₂)(PEtPh₂)₃ complex, 2000 cm⁻¹ is a very safe upper limit on the dynamically relevant energy range. That said, there is some interest in the higher-lying rotational states as well, as these may be relevant for more energetic processes. Besides the H₂–H–H exchange

reaction already discussed, there might be coupling with the first H_2 stretch excitation—which, in a different Fe compound, was found to lie at 2973 cm⁻¹ above the ground state.⁴⁸ A similar "softening" of the H_2 vibrational frequency can be expected in Fe(H)₂(H₂)(PEtPh₂)₃. It is perhaps noteworthy that we have discovered a Fermi resonance in this spectral region around 2500 cm⁻¹—although only for the relaxed PES, not for the frozen PES.

In any event, the frozen PES developed here yields *excellent* agreement with all available experimental transition frequencies⁴²—e.g., subwavenumber for the ground state tunneling splitting, and ~10 cm⁻¹ or better for the next higherlying *ortho*-H₂ and *para*-H₂ transitions (note that for neutron scattering, both are symmetry-allowed). This is all the more remarkable, considering that our calculation is purely *ab initio*, with no (semi)-empirical corrections of any kind. On the other hand, given that the frozen PES fitting errors are themselves a few cm⁻¹, throughout the dynamically relevant space, some of this agreement may be fortuitous. In any case, the present success certainly seems to validate our QD methodology and bodes very well for future studies of this kind

More specifically, within the general context of hydrogen ligand QD, the lessons suggested by the present study can be summarized as follows: (1) the frozen substrate model works much better than the relaxed substrate model; (2) the choice of DFT functional, basis set, etc. is less important than the dynamical model, e.g. frozen vs. relaxed; (3) all H-atom d.o.f.'s must be treated explicitly quantum mechanically; (4) gas-phase calculations can do a reasonable job of mimicking crystal experiments, provided that the local structure is similar. Regarding (3), it seems clear that even relatively small coupling across d.o.f.'s of the type observed here can result in very significant QD effects. In particular, tunneling splittings are notoriously difficult to compute accurately, in part, because they depend sensitively on even small couplings of this kind. For the Fe(H)₂(H₂)(PEtPh₂)₃ system, for example, all previous 1-D calculations overestimated the ground state tunneling splitting because the θ - ϕ correlation that was ignored acts as if to increase the azimuthal barrier height.⁵⁸

On the other hand, QD quantities such as tunneling splittings are probably much *more* forgiving with respect to variation of the equilibrium structure—at least insofar as the H-atom coordinates are concerned. This, of course, reflects the highly delocalized nature of the hydrogen, which naturally tends to average over small features of the PES. The precise location of the global minimum geometry therefore may not matter very much, particularly if the PES is quite flat, or has small barriers, as is the case here.

SUPPLEMENTARY MATERIAL

See supplementary material for the following: raw *ab initio* data for both the relaxed and frozen PESs; comprehensive list of all computed energy levels for the relaxed and frozen PESs; wavefunction density plots for many high-lying states, for the frozen PES.

ACKNOWLEDGMENTS

This work was largely supported by both a research grant (No. CHE-1665370) and a CRIF MU instrumentation grant (No. CHE-0840493) from the National Science Foundation. Additional support from the Robert A. Welch Foundation (No. D-1523) is also acknowledged. We also gratefully acknowledge the following entities for providing access and technical support for their respective computing clusters: the Texas Tech University High Performance Computing Center, for use of the Hrothgar facility; the Texas Tech University Department of Chemistry and Biochemistry, for use of the Robinson cluster. Additionally, Dr. Rene F. K. Spada is acknowledged for providing the program to generate structures for DFT calculations.

- ¹H. Berke, Chem. Phys. Chem. **11**, 1837 (2010).
- ²N. L. Rosi, J. Eckert, M. Eddaoudi, D. T. Vodak, J. Kim, M. O'Keefe, and O. M. Yaghi, Science 300, 1127 (2003).
- ³P. D. C. Dietzel, P. A. Georgiev, J. Eckert, R. Blom, T. Strässle, and T. Unruh, Chem. Commun. **46**, 4962 (2010).
- ⁴See http://energy.gov/eere/fuelcells/hydrogen-storage for Hydrogen Storage; accessed 24 July 2016.
- ⁵L. J. Murray, M. Dincă, and J. R. Long, Chem. Soc. Rev. **38**, 1294 (2009).
- ⁶K. Sumida, D. Stück, L. Mino, J.-D. Chai, E. D. Bloch, O. Zavorotynska, L. J. Murray, M. Dincă, S. Chavan, S. Bordiga, M. Head-Gordon, and J. R. Long, J. Am. Chem. Soc. **135**, 1083 (2013).
- ⁷G. J. Kubas, R. R. Ryan, B. I. Swanson, P. J. Vergamini, and H. J. Wasserman, J. Am. Chem. Soc. **106**, 451 (1984).
- 8See http://energy.gov/eere/fuelcells/metal-hydride-storage-materials for Metal Hydride Storage Materials; accessed 24 July 2016.
- ⁹G. J. Kubas, Proc. Natl. Acad. Sci. U. S. A. **104**, 6901 (2007).
- ¹⁰G. J. Kubas, Catal. Lett. **104**, 79 (2005).
- ¹¹J. Eckert and W. Lohstroh, in *Neutron Applications in Materials for Energy*, edited by G. J. Kearley and V. K. Peterson (Springer, Berlin, 2015), Chap. 8.
- ¹²G. J. Kubas, Chem. Rev. **107**, 4152 (2007).
- ¹³D. M. Heinekey, A. Lledos, and J. M. Lluch, Chem. Soc. Rev. 33, 175 (2004).
- ¹⁴N. Došlić, V. Gomzi, M. Mališ, I. Matanović, and J. Eckert, Inorg. Chem. 50, 10740 (2011).
- ¹⁵L. Wang, N. R. Stuckert, H. Chen, and R. T. Yang, J. Phys. Chem. C 115, 4793 (2011).
- ¹⁶K. Lin, A. K. Adhikari, K. Chang, M. Tu, and W. Lu, Cat. Today **164**, 23 (2011).
- ¹⁷L. Morris, M. L. Trudeau, D. Reed, D. Book, and D. M. Antonelli, Chem. Phys. Chem. **17**, 778 (2016).
- ¹⁸B. Poirier and J. McAfee, J. Chem. Phys. **134**, 074308 (2011).
- ¹⁹B. Poirier and J. McAfee, J. Chem. Phys. **130**, 064701 (2009).
- ²⁰A. C. Dillon, K. M. Jones, T. A. Beckkedahl, C. H. Kiang, D. S. Bethune, and M. J. Heben, Nature 386, 377 (1997).
- ²¹P. Chen, X. Wu, J. Lin, and K. Tan, Science **285**, 91 (1999).
- ²²B. Chambers, C. Park, R. Baker, and N. Rodriquez, J. Phys. Chem. B **102**, 4253 (1998).
- ²³R. Yang, Carbon **38**, 623 (2000).
- ²⁴L. Zhou, Y. Zhou, and Y. Sun, Int. J. Hydrogen Energy **29**, 319 (2004).
- ²⁵ A. Nikitin, H. Ogasawara, D. Mann, R. Denecke, Z. Zhang, H. Dai, K. Cho, and A. Nilsson, Phys. Rev. Lett. 95, 225507 (2005).

- ²⁶ A. Nikitin, X. Li, Z. Zhang, H. Ogasawara, H. Dai, and A. Nilsson, Nano Lett. 8, 162 (2008).
- ²⁷S. Han and H. Lee, Carbon **42**, 2169 (2004).
- ²⁸T. Pham, K. Forrest, B. Space, and J. Eckert, Phys. Chem. Chem. Phys. 18, 17141 (2016).
- ²⁹J. Eckert, A. Albinati, R. P. White, C. Bianchini, and M. Peruzzini, Inorg. Chem. 31, 4241 (1992).
- ³⁰J. Eckert, H. Blank, M. T. Bautista, and R. H. Morris, Inorg. Chem. 29, 747 (1990).
- ³¹H.-H. Limbach, S. Ulrich, S. Gründemann, G. Buntkowsky, S. Sabo-Etienne, B. Chaudret, G. J. Kubas, and J. Eckert, J. Am. Chem. Soc. 120, 7929 (1998).
- ³²J. Eckert, G. J. Kubas, J. H. Hall, P. J. Hay, and C. M. Boyle, J. Am. Chem. Soc. **112**, 2324 (1990).
- ³³G. J. Kubas, R. R. Ryan, and C. J. Unkefer, J. Am. Chem. Soc. **109**, 8113 (1987).
- ³⁴J. Tomàs and A. Lledòs, Organometallics 17, 190 (1998).
- ³⁵R. H. Morris, J. F. Sawyer, M. Shiralian, and J. D. Zubkowski, J. Am. Chem. Soc. **107**, 5581 (1985).
- ³⁶G. Khalsa, K. Rattan, G. J. Kubas, C. J. Unkefer, L. S. Van Der Sluys, and K. A. Kubat-Martin, J. Am. Chem. Soc. 112, 3855 (1990).
- ³⁷S. Li, M. B. Hall, J. Eckert, C. M. Jensen, and A. Albinati, J. Am. Chem. Soc. **122**, 2903 (2000).
- ³⁸C. Scheurer, R. Wiedenbruch, R. Meyer, and R. R. Ernst, J. Chem. Phys. 106, 1 (1997).
- ³⁹E. Clot and J. Eckert, J. Am. Chem. Soc. **121**, 8855 (1999).
- ⁴⁰J. Eckert and G. J. Kubas, J. Phys. Chem. **97**, 2378 (1993).
- ⁴¹I. Matanovic, J. L. Belof, B. Space, J. Sauer, J. Eckert, and Z. Bacic, J. Chem. Phys. **137**, 014701 (2012).
- ⁴²L. S. Van Der Sluys, J. Eckert, O. Eisenstein, J. H. Hall, J. C. Huffman, S. A. Jackson, T. F. Koetzle, G. J. Kubas, P. J. Vergamini, and K. G. Caulton, J. Am. Chem. Soc. 112, 4831 (1990).
- ⁴³J.-F. Riehl, M. Pelissier, and O. Eisenstein, Inorg. Chem. **31**, 3344 (1992).
- ⁴⁴K. W. Zilm, M. D. Heinekey, J. M. Millar, N. G. Payne, S. P. Neshyba, J. C. Duchamp, and J. Szczyrba, J. Am. Chem. Soc. 112, 920 (1990).
- ⁴⁵D. C. Harris and M. D. Bertolucci, *Symmetry and Spectroscopy: An Introduction to Vibrational and Electronic Spectroscopy* (Dover Publications, Inc., New York, 1978), pp. 168–170.
- ⁴⁶R. M. Dimeo, Am. J. Phys. **71**, 885 (2003).
- ⁴⁷ K. Yagi, G. V. Mil'nikov, T. Taketsugu, K. Hirao, and H. Nakamura, Chem. Phys. Lett. **397**, 435 (2004).
- ⁴⁸G. E. Gadd, R. K. Upmacis, M. Poliakoff, and J. J. Turner, J. Am. Chem. Soc. **108**, 2547 (1986).
- ⁴⁹G. J. Kubas, C. J. Unkefer, B. I. Swanson, and E. Kukushima, J. Am. Chem. Soc. 108, 7000 (1986).
- ⁵⁰ W. J. Oldham, Jr., A. S. Hinkle, and D. M. Heinekey, J. Am. Chem. Soc. 119, 11028 (1997).
- ⁵¹M. Arresta, P. Giannoccaro, M. Rossi, and A. Sacco, Inorg. Chim. Acta 5, 115 (1971).
- ⁵²A. D. Becke, J. Chem. Phys. **98**, 5648–5652 (1993).
- ⁵³C. T. Lee, W. T. Yang, and R. G. Parr, Phys. Rev. B **37**, 785–789 (1988).
- ⁵⁴A. Schäfer, H. Horn, and R. Ahlrichs, J. Chem. Phys. **97**, 2571 (1992).
- ⁵⁵M. Dolg, U. Wedig, H. Stoll, and H. Preuss, J. Chem. Phys. **86**, 866 (1987).
- ⁵⁶TURBOMOLE V7.0 2015, a development of University of Karlsruhe and Forschungszentrum Karlsruhe GmbH, 1989-2007, TURBOMOLE GmbH, since 2007; available from http://www.turbomole.com.
- ⁵⁷M. Rose, *Elementary Theory of Angular Momentum* (Dover Publications, Inc., New York, 1995).
- ⁵⁸B. Poirier, Phys. Rev. A **56**, 120 (1997).